4-1-2018

Soot and Spectral Radiation Modeling for High-Pressure Turbulent Spray Flames

Sebastian Ferreyro Fernandez
The Pennsylvania State University

C. Paul
The Pennsylvania State University

A. Sircar
The Pennsylvania State University

A. Imren
The Pennsylvania State University

D. C. Haworth
The Pennsylvania State University

See next page for additional authors

Accepted version. *Combustion and Flame*, Vol. 190 (April 2018): 402-415. DOI.

Combustion and Flame, Vol.1 90, (April, 2018). DOI.

Contents

Soot and spectral radiation modeling for high-pressure turbulent spray flames

Sebastian Ferreyro Fernandez
The Pennsylvania State University, University Park, PA
C. Paul
The Pennsylvania State University, University Park, PA
A. Sircar
The Pennsylvania State University, University Park, PA
A. Imren
The Pennsylvania State University, University Park, PA
D. C. Haworth
The Pennsylvania State University, University Park, PA
S. Roy
Marquette University, Milwaukee, WI
M. F. Modest
University of California, Merced, CA

Abstract

A transported probability density function (PDF) method and a photon Monte Carlo/line-by-line (PMC/LBL) spectral model are exercised to generate physical insight into soot processes and spectral radiation characteristics in transient high-pressure turbulent n-dodecane spray flames, under conditions that are relevant for compression-ignition piston engines. PDF model results are compared with experimental measurements and with results from a locally well-stirred reactor (WSR) model that neglects unresolved turbulent fluctuations in composition and temperature. Computed total soot mass and soot spatial distributions are highly sensitive to the modeling of unresolved turbulent fluctuations. To achieve reasonable agreement between model and experiment and to capture the highly intermittent nature of soot in the turbulent flame, it is necessary to accurately represent mixing and the low diffusivity of soot particles. This is accomplished in the PDF framework using a mixing model that enforces locality in the gas-phase composition space, while not mixing the transported soot variables. The results suggest that mixing is at least as important as kinetics in controlling soot formation and evolution in high-pressure turbulent flames. Regarding radiation, radiant fractions and global influences of radiation in these flames are relatively small. Nevertheless, an examination of spectral radiative heat transfer provides valuable insight into the nature and modeling of radiation in high-pressure turbulent combustion systems. There are complex spectral interactions that are revealed using PMC/LBL. CO_2 dominates the total radiative emission and reabsorption, but most of the emitted CO_2 radiation is reabsorbed before reaching the walls. On the other hand, most of the emitted soot radiation reaches the walls, but soot radiation is a small contribution overall; H_2O dominates the radiation that reaches

the walls. Global turbulence–radiation interactions (TRI) effects are small, but radiative emission from soot increases by approximately a factor two when TRI are considered. Radiative transfer contributes both to energy redistribution in the vessel and to wall heat losses. The results suggest that a simple model that considers soot radiation and the principal CO_2 and H_2O spectral bands might be sufficient to capture the key influences of radiation in engine CFD. It is expected that these findings will contribute to the development of truly predictive CFD models for engines and other high-pressure turbulent combustion systems.

Keywords

Computational fluid dynamics; Soot; Spectral radiation; Compression-ignition engine; PDF method

1. Introduction

Compression-ignition piston engines are widely used in applications including transportation, construction, farming and electric power generation. Increasingly stringent regulations on fuel consumption and emissions are driving the development of next-generation engines that aim to simultaneously achieve high reliability, low maintenance, low fuel consumption and low pollutant emissions.[1] Advanced and truly predictive computational fluid dynamics (CFD)-based models are needed to achieve these goals.[2] Key physical processes to be modeled include liquid fuel injection and spray processes, autoignition and turbulent combustion, heat transfer, and pollutant formation.

In this paper, two important and related aspects are addressed: soot formation/evolution, and spectral radiative heat transfer. Soot modeling for engine-relevant conditions has received considerable attention, because of the importance of soot as a component of particulate matter, a regulated pollutant. However, soot modeling remains a weak link in engine CFD. Most soot models are based largely on physical understanding of soot processes derived from experiments at atmospheric pressure or at moderately elevated pressures (usually less than 10 atm) compared to engine-relevant conditions, and the emphasis has been on soot kinetics rather than on turbulent hydrodynamics and mixing. On the other hand, radiative heat transfer modeling in engines has received relatively little attention, although it is increasingly recognized that it can be important both for energy redistribution within the combustion chamber and as a contributor to wall heat losses.[3,4] Conventional wisdom has been that radiative heat transfer in engines is dominated by soot radiation. However, as operating pressures and exhaust-gas recirculation (EGR) levels in engines increase, and as combustion systems are designed to produce less in-cylinder soot, molecular gas radiation (primarily from CO_2 and H_2O) and spectral radiation properties become more important.

To make progress toward unraveling the complex underlying physical processes and developing reliable CFD models, it is expedient to consider configurations that are more amenable to modeling and experiment compared to a practical engine. To this end, the Engine Combustion Network (ECN)[5] was established to provide an open forum for international collaboration among experimental and computational researchers in engine combustion. One target configuration is a constant-volume turbulent spray combustion chamber that can reach thermochemical conditions (composition, temperature and pressure) that are representative of those in modern direct-injection compression-ignition engines, while allowing a high degree of optical access for advanced experimental diagnostics and well-characterized initial and boundary conditions for CFD, including detailed fuel-injector characterization.[5,6,7]

Here ECN “Spray A” (liquid n-dodecane fuel) is targeted. A transported probability density function (PDF) method is used to account for the influences of unresolved turbulent fluctuations in composition and temperature on chemistry (turbulence–chemistry interactions – TCI) and on radiation (turbulence–radiation interactions – TRI), and a photon Monte Carlo (PMC) method with line-by-line (LBL) spectral resolution is used for spectral radiative transfer. Several earlier modeling studies have been published for Spray A, and an up-to-date summary can be found at.[8] Most relevant to the current work are studies that focused on turbulence–chemistry interactions using transported PDF methods.[9,10,11] including soot and radiation.[12] Results obtained here will be compared with experimental measurements and with results from earlier modeling studies in the Results and Discussion section.

The main contributions of this paper are: 1) to confirm the importance of turbulence–chemistry interactions in high-pressure turbulent flames, and to demonstrate that they are especially important for soot formation and evolution; 2) to show that with appropriate treatment of unresolved turbulent fluctuations, a RANS-based model can capture soot intermittency and related effects; 3) to provide evidence that turbulent transport and mixing are at least as important as kinetics in governing soot formation and evolution in high-pressure turbulent flames, such as in engines; 4) to show that consideration of spectral radiative properties is essential to understanding radiative transfer in engine-relevant environments; and 5) to propose key ingredients that should be included in a CFD-based model for radiative transfer in engines. These are expected to contribute to the development of truly predictive CFD-based models of in-cylinder processes in engines and other high-pressure turbulent combustion systems.

2. Target flames

The experimental configuration is a constant-volume, optically accessible, cubic spray combustion vessel with an enclosed volume of 1147 cm^3. The vessel is capable of accessing a wide range of engine-relevant thermochemical conditions, allowing initial temperatures up to 1400 K, pressures up to 350 MPa and different levels of oxygen and simulated EGR gases. The desired pre-fuel-injection (“ambient”) conditions are varied by preburning a combustible mixture. For this purpose, two spark plugs and a mixing fan are mounted on one wall of the vessel. Further description of the experimental setup can be found in.[7] This is one of the ECN target configurations.[5]

Here simulations of ECN Spray A are reported.[8] Liquid sprays of n-dodecane ($C_{12}H_{26}$) are injected using a common-rail diesel-engine fuel injector with a single orifice of nominal diameter 90 µm, located at the center of one vessel wall and injecting toward the center of the vessel. In all cases, the initial chamber gas density is 22.8 kg/m^3, the liquid fuel injection pressure is 150 MPa, and the injection duration is 5.5 ms. For reacting cases, the ambient gas composition includes 15% O_2 with the remainder being N_2 (75.15%), CO_2 (6.22%) and H_2O (3.62%), and the ambient temperature ranges from 750 K to 1200 K. The baseline Spray A case corresponds to an ambient gas temperature of 900 K, and this is the condition that is analyzed most extensively in this paper. Reacting experimental data include ignition delays and lift-off lengths, total soot mass as a function of time after start of injection (SOI) and spatial distributions of soot volume fraction,[13] and radiant fractions and spatially and spectrally resolved radiative intensities.[14]

For the nonreacting case, the ambient gas composition is pure N_2 and the ambient temperature is 900 K. In the experiments, the same fuel-injector nozzle was used for all reacting cases (#210370), while a different (nominally identical) nozzle was used for the nonreacting case (#210677). Nonreacting

experimental data include liquid and vapor penetration as functions of time, and spatial distributions of mixture fraction (fuel mass fraction) at different times after SOI.[7,15]

3. Physical models and numerical methods

An unsteady Reynolds-averaged Navier–Stokes (URANS) formulation is adopted, using solvers based on the OpenFOAM v2.3.x toolbox.[16] A segregated pressure-based finite-volume method is used to solve the coupled mean momentum, pressure and enthalpy equations, with second-order spatial discretizations and first-order implicit time discretization. The baseline physical models and model coefficients are summarized in Table 1.

Table 1. Summary of baseline physical models.

Physical Process	**Formulation [ref.]**	**Model(s) [Refs.]**	**Coefficient Values**
Turbulence	URANS	$k-\varepsilon$[17]	$C_\mu = 0.09,$ $C_{\varepsilon 1} = 1.55,$ $C_{\varepsilon 2} = 1.92,$ $C_{\varepsilon 3} = -0.33,$ $\sigma_k = 1.00,$ $\sigma_\varepsilon = 1.30,$
	Stochastic	Blob injection/atomization [19,20]	LBU=1.0
Fuel Spray	Lagranfgian Parcel[21]	Reitz-Diwakar secondary breakup [22,23,24]	$C_{bag} = 6.0,$ $C_b = 0.785,$ $C_{strip} = 0.5,$ $C_8 = 9.0,$
Gas-phase	Ideal-gas		
Thermo-	Mixture	54-species n-dodecane [25]	See[25]
Chemistry			
	Continuum	Semi-empirical	
Soot	Species	Two-equation[26]	See[26]
	Equations	Soot oxidation from [27]	See [27]
	Lagrangian	Gradient transport	$\sigma_\emptyset = 1.0,$
TCI	Particle	EMST mixing [28]	$C_\emptyset = 1.5,$
	Composition	No mixing for soot	
	PDF [29]		

A two-equation k-ε turbulence model is used.[17] The model coefficients are C_μ (multiplies k^2/ε to give the apparent turbulent viscosity), $C_{\varepsilon 1}$, $C_{\varepsilon 2}$ and $C_{\varepsilon 3}$ (coefficients in the modeled ε equation), and σ_k and σ_ε (turbulent Schmidt numbers in the k and ε equations, respectively). Standard values are used for all coefficients except $C_{\varepsilon 1}$, for which a simple round-jet correction has been used (value increased from 1.44 to 1.55[18]).

The liquid fuel injection and spray evolution are modeled using a stochastic Lagrangian parcel method.[21] The spray is represented by a finite number of parcels, where each parcel represents a group of droplets having the same properties. A simple blob model is employed to represent spray atomization,[19,20] and the Reitz–Diwakar model is used for secondary breakup.[22,23] These models are not considered to be truly predictive; rather, the models are tuned to match the measured liquid and vapor penetration rates for the nonreacting case (see Section 4.1 below). The atomization model coefficient *LBU* is related to the distance from the fuel nozzle where the secondary breakup model is switched on, and a standard value of 1.0 has been used. The secondary breakup model coefficients are: critical Weber number for bag-type breakup C_{bag}, time factor for bag-type breakup C_b, Weber number factor for stripping-type breakup C_{strip}, and time factor for stripping-type breakup C_s. Standard values have been used for all coefficients except C_s, which was reduced from 10.0 to 9.0 to better match the experimental liquid penetration. The lower value of C_s increases the rate at which smaller droplets are formed from the breakup of larger droplets, thereby reducing the liquid penetration. This value of C_s is still within the range that is typically used for modeling high-pressure diesel sprays.

For the gas phase, a chemically reacting ideal-gas mixture is considered. The baseline chemical mechanism is a 54-species, 269-reaction skeletal n-dodecane mechanism.[25] This mechanism was developed to predict pyrolysis and oxidation of n-dodecane at low and high temperatures. Low-temperature reaction rates were tuned against a detailed mechanism[30] and experimental data, including Spray A. The mechanism showed good agreement for ignition delay and lift-off length in previous Spray A simulations.[13,25] Some results obtained using a different chemical mechanism[31] are included, for comparison purposes. The second mechanism consists of a main mechanism of 96 species, appended with a submechanism of 37 species for polycyclic aromatic hydrocarbons (PAHs): 133 total species. Spray A was not one of the target flames used in the 133-species mechanism development. In all cases, the stiff ODE solver presented in[32] is used to integrate the chemical source terms.

The baseline soot model is the semi-empirical two-equation model proposed in.[26] For this model, two additional modeled “species” equations are solved for soot mass fraction and particle number density. The model includes representations for particle inception, surface growth, oxidation and coagulation. Inception is based on acetylene (C_2H_2), which makes the model suitable for chemical mechanisms that do not include PAHs. Soot oxidation pathways were augmented to consider oxidation by OH and O (in addition to O_2), with the addition of the two reactions suggested in.[27]

Some results obtained using a more detailed soot model based on the method of moments with interpolative closure (MOMIC)[33] are included, for comparison purposes. This allows more information about the soot particle size distribution to be represented, compared to the baseline two-equation soot model that assumes a uniform particle size distribution. In the present MOMIC implementation, equations are solved for the first six moments of the number of carbon atoms. Physically, the moment of order zero represents the particle number density and the moment of order one is related to the soot mass fraction. Here pyrene is used as soot precursor species instead of acetylene, and the same surface chemistry mechanisms are used as in the baseline two-equation soot model.

One-way coupling between the gas phase and soot (no consumption or production of gas-phase species involved in soot processes) is used for the C_2H_2/two-equation model, while two-way coupling is used for the PAH/MOMIC model. This is based on findings from our earlier modeling studies of laminar and turbulent flames (e.g.,[34]). These studies found that it is important to account for PAH consumption when

using PAH-based models, while results obtained using C_2H_2-based models change little with consideration of two-way coupling. The reason is essentially the higher concentrations of C_2H_2 that are usually present, compared to PAHs. Typically only a small fraction of the available C_2H_2 is consumed to form soot, whereas a significant fraction of the available PAH can be consumed.

The influence of unresolved turbulent fluctuations in composition and temperature on combustion (turbulence–chemistry interactions – TCI) are accounted for using a transported probability density function (PDF) method. The PDF considered is the joint composition PDF of gas-phase species composition, soot model quantities and mixture specific enthalpy. With N_S denoting the number of species in the gas-phase chemical mechanism and N_{soot} the number of transported quantities in the soot model, this is a $(N_s + N_{soot} + 1)$ –dimensional PDF (excluding spatial and temporal dependencies). The modeled PDF equation is solved using a consistent hybrid Lagrangian particle/Eulerian mesh method,[29] where the number of notional PDF particles per finite-volume cell is controlled to remain between 50 and 100. Key models required are a model to account for transport by turbulent velocity fluctuations, and a model to account for molecular transport ("mixing"). For the former, a gradient transport assumption is made, with a constant apparent turbulent Schmidt number σ_ϕ. For mixing, the Euclidean minimum spanning tree (EMST) model is used,[28] with a constant value of the model coefficient C_ϕ. To account for the essentially zero molecular diffusivity (high Schmidt number) of soot particles, EMST is used only for the gas-phase compositions and mixture-specific enthalpy, while soot model variables are not mixed. Standard values are used for both model coefficients. As will be seen in Section 4, the treatment of mixing has a significant influence on soot formation and evolution. An important feature of EMST is that it enforces locality of mixing in the gas-phase composition space. To demonstrate the importance of mixing on soot formation and evolution, some results are presented for different values of C_ϕ, for a different mixing model (interaction by exchange with the mean – IEM[35]), and for a case where soot variables are mixed in addition to gas-phase compositions. Finally, to demonstrate the importance of unresolved turbulent fluctuations, results obtained using the PDF-based model are compared with those obtained using a model that neglects turbulent fluctuations altogether: a locally well-stirred reactor – WSR – model. In that case, chemical source terms are computed using local mean values of composition and temperature, rather than notional PDF particle values.

A hierarchy of spectral radiation models and radiative transfer equation (RTE) solvers has been implemented.[36] Here the statistical photon Monte Carlo (PMC) method with line-by-line (LBL) spectral resolution has been used.[37,38] in a post-processing mode. In PDF/PMC, notional photon bundles are launched from each notional PDF particle (emission), where the direction, wavenumber, and energy of each bundle are assigned using random-number relations that are consistent with the local radiative properties of the mixture. Each bundle is traced through the medium, and loses an appropriate amount of energy to each notional PDF particle with which it interacts (reabsorption), based on the local radiative properties. Tracing continues until the bundle's energy is depleted, or it leaves the computational domain. Scattering can be accommodated through additional statistical rules by which the direction of each bundle would change, but scattering has been neglected here. Scattering by soot particles is expected to be negligible, as discussed in Chapter 11 of.[37]

Because radiation is computed using notional PDF particle compositions and temperature, the influences of unresolved turbulent fluctuations on radiation (turbulence–radiation interactions – TRI) are captured in natural way. Alternatively, radiative emission and reabsorption can be computed using

local mean values of composition and temperature, thereby neglecting TRI. Both methods are used here, to isolate and quantify the importance (or lack thereof) of TRI.

In contrast to other RTE solution methods, PMC invokes no intrinsic approximations regarding the directional variation of radiative intensity. The method is exact (within the limits of statistical error), to the extent that the radiative properties of the medium are known. Here three participating molecular gases are considered (CO_2, H_2O and CO), and their LBL spectral radiative properties are taken from the HITEM2010 database.[39] For soot particles, the small-particle (Rayleigh) limit is considered, and the correlation given in[40] is used for the wavenumber-dependent complex index of refraction. The wavelength range considered is 670–50,000 nm for gas-phase species, and 400–30,000 nm for soot. The soot wavelengths were extended further into the visible to enable quantitative comparisons between computed and measured spectral intensities, which will be shown later. The index of refraction of soot particles has been the subject of extensive research, and several different values have been published. A review can be found in Chapter 11 of.[37] There it is shown that at wavelengths of interest for heat transfer, the value of the spectral absorption coefficient for soot particles can vary by as much as a factor of two, depending on the value of the index of refraction that is used. A factor of two change in the absorption coefficient for soot would change the quantitative results presented in Section 4.4 below, but would not alter any of the general conclusions that are drawn.

The computational domain is a two-dimensional (axisymmetric) wedge mesh that represents a 5° section of the entire vessel. The axial (*z*) and radial (*r*) extents of the domain are 108 mm (same as in the experiment) and 58 mm (to give the same total vessel volume as in the experiment), respectively. The fuel injector orifice is at z=r=0, and fuel is injected in the +z direction. The mesh consists of 12,800 nonuniformly distributed hexahedral cells, with higher resolution close to the fuel injector orifice. The minimum grid size is approximately 0.25 mm. Homogeneous initial conditions are assumed, with the composition and temperature taken to be that of the nominal ambient mixture, and with zero mean velocity. The initial turbulence kinetic energy and turbulence dissipation rate were adjusted to match the vapor penetration profile in the nonreacting case: $k_0 = 0.25\ m^2/S^2$ and $\varepsilon_0 = 41.0\ m^2/S^2$, which correspond to an rms turbulence velocity of m/s and a turbulence length scale of $l_t = 0.5\ mm$. Injection mass flow rate profiles were obtained from.[41] Symmetry conditions are applied on all boundaries except those corresponding to solid walls, where no-slip conditions and standard wall functions are used, with wall temperatures set to 50 K below the gas ambient temperature. The computational time step is 5.0×10^{-7} s.

4. Results and discussion

The same approach has been followed here as that used in earlier URANS modeling studies of transient autoignition and combustion for the ECN high-pressure turbulent spray flames. The turbulence model (including initial conditions) and liquid fuel injection/spray models are adjusted to give an acceptable level of agreement between computed and measured liquid and vapor penetration and mixture fraction (fuel mass fraction) profiles for the nonreacting case. That is how the coefficient values reported in Table 1 were established. These models are applied without further adjustment to simulate reacting cases using the selected chemical mechanism(s) and turbulence–chemistry interaction model(s), with appropriate changes to the ambient mixture composition and temperature. The models are then exercised to generate insight into the physical processes of interest: here, soot formation/evolution and spectral radiative heat transfer.

4.1. Nonreacting case

Computed liquid and vapor penetration were extracted following definitions recommended in the latest ECN Workshop (ECN5).[42] The liquid penetration length is defined as the distance from the fuel nozzle exit to the farthest axial position encompassing 99% of the injected fuel mass. Vapor penetration length is defined as the distance along the nozzle axis from the nozzle exit to where the mixture fraction (fuel mass fraction) falls to 0.1%.

Figure 1a shows computed and measured liquid and vapor penetration lengths as functions of time after start of injection (SOI). Results from the WSR and PDF models are essentially the same, as expected for nonreacting cases. The level of agreement between models and experiment is similar to what has been reported in other modeling studies,[8,42] and is satisfactory for the purposes of this paper. Computed and measured radial profiles of mean and rms mixture fraction at an instant 1.5 ms after SOI are shown in Fig. 1b and c. Again, the WSR and PDF models give essentially the same mean profiles, which are close to the lower edge of the measured envelope near the centerline. The level of rms fluctuations predicted by the PDF model is in good agreement with experiment; no estimate of the fluctuations was extracted from the WSR model. The computed mean mixture fraction profiles could be brought into somewhat better agreement with experiment with further tuning of the turbulence model, but the nonreacting results are satisfactory for the present purposes.

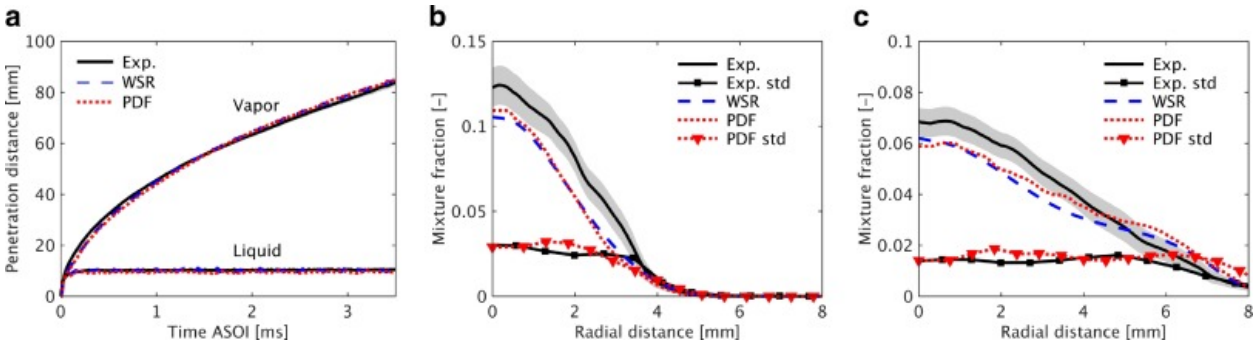

Fig. 1. Comparisons between measurements and simulations (WSR and PDF models) for the nonreacting case. a) Liquid and vapor penetration as functions of time. b) and c) Radial profiles of mean and rms mixture fraction 1.5 ms after SOI, 25 mm (in b) and 45 mm (in c) downstream of the injector nozzle. The shaded region around the experimental mean mixture fraction profile shows the reported measurement uncertainty.

4.2. Reacting cases: ignition delay and lift-off length

Computed and measured ignition delays and lift-off lengths as functions of ambient temperature are compared in Fig. 2. For both quantities, the ECN5 recommendations[42] have been followed. Ignition delay is defined as the first instant at which the Favre-averaged OH mass fraction reaches 2% of the maximum value in the domain after a stable flame is established. The lift-off length is defined as the axial location in the quasi-stationary flame where the Favre-averaged OH mass fraction first reaches 14% of its maximum value in the domain. Computed results are shown for two chemical mechanisms, each with (PDF) and without (WSR) consideration of turbulence–chemistry interactions.

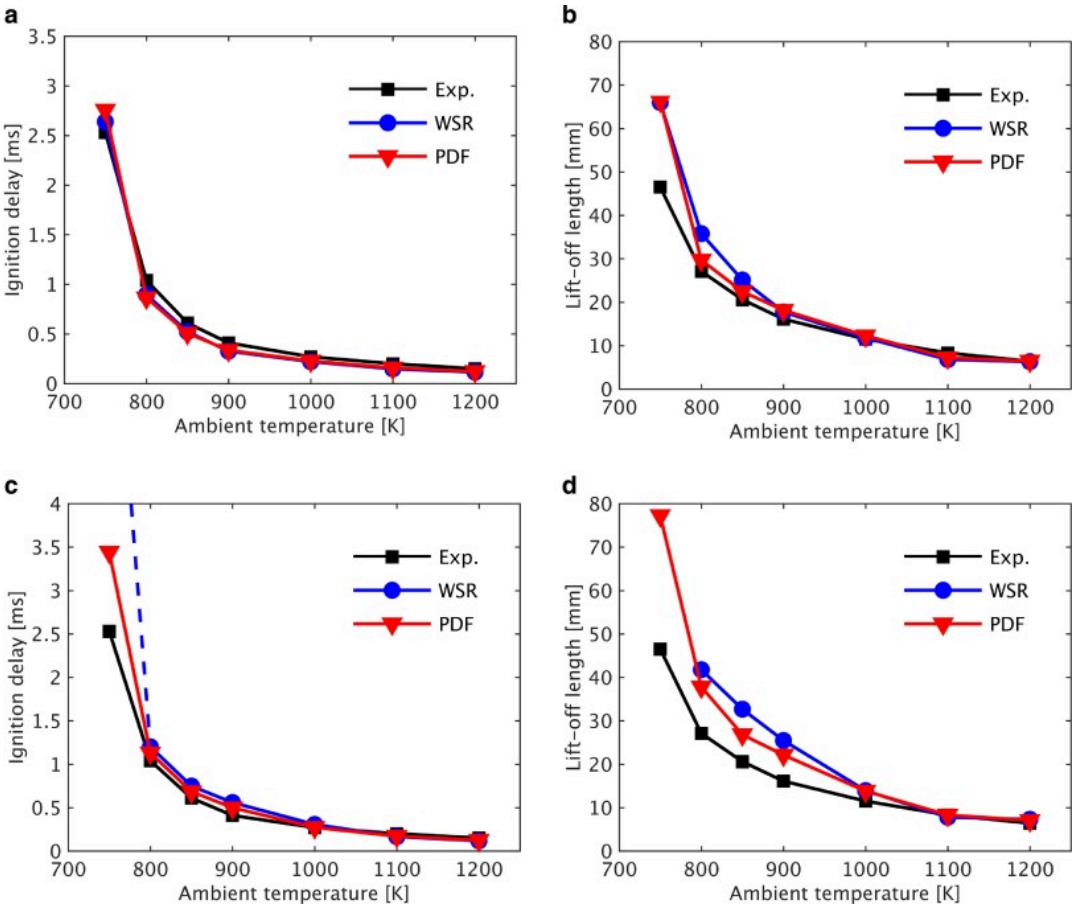

Fig. 2. Measured and computed (using WSR and PDF models) ignition delays and lift-off lengths versus ambient temperature for the reacting cases. a) Ignition delay for the 54-species mechanism. b) Lift-off length for the 54-species mechanism. c) Ignition delay for the 133-species mechanism; the WSR model fails to ignite for the 750 K ambient temperature case. d) Lift-off length for the 133-species mechanism.

For the baseline 54-species chemical mechanism, WSR and PDF computed ignition delays are within 10% of one another and of experiment, for all ambient temperatures. This mechanism was essentially tuned to match measured ignition delays for Spray A without consideration of turbulence-chemistry interactions, and the results reflect that. WSR and PDF computed lift-off lengths are within a few percent of each other and of experiment for ambient temperatures ≥ 900 K. The PDF model gives shorter lift-off lengths that are in closer agreement with experiment compared to the WSR model for 800 K and 850 K, but for 750 K, the PDF lift-off length is slightly longer than the WSR value. This may be attributed to the high level of noise in computed OH for the PDF model at this low ambient temperature, where the OH levels are low. Aside from the anomalous PDF lift-off length for 750 K, these results are largely consistent with what has been reported by other groups using this chemical mechanism for the ECN n-dodecane sprays.[42]

In contrast to the 54-species mechanism, the 133-species mechanism was not developed specifically with Spray A autoignition as a target. Rather, it was developed to give improved PAH predictions. For the 133-species mechanism, computed ignition delays and lift-off lengths show larger influences of turbulence–chemistry interactions at lower ambient temperatures. For the 750 K ambient temperature, the WSR model fails to ignite altogether; the PDF model does ignite, but the computed lift-off length is

more than 50% higher than the measured value. The difficulties of accurately predicting low-temperature and negative-temperature-coefficient behavior are well known, and are discussed in,[25,30,31] for example. A detailed analysis of Spray A turbulent flame structure at ambient temperatures of 800 K, 900 K and 1100 K can be found in.[11] Here there is evidence of first-stage ignition (formaldehyde production) in all cases. In cases that reach second-stage (main) ignition, the total formaldehyde in the computational domain peaks, then drops at the time corresponding to main ignition, where non-negligible OH first appears. For the 133-species mechanism WSR model at 750 K, the formaldehyde continuously increases over the time of the simulation, and OH never reaches non-negligible levels. Detailed analysis of the ignition behavior at low temperature is beyond the scope of this paper, and is probably not warranted in any case for the chemical mechanisms used here. Here the focus is on soot and radiation at higher ambient temperatures. At higher ambient temperatures, the relative importance of turbulent fluctuations on global ignition behavior is smaller than at lower ambient temperatures, since the air–fuel-ratio range over which the mixture reacts is wider at higher temperatures.

The general trends in Fig. 2 are qualitatively consistent with what was observed in[9] (using the chemical mechanism from[43]) and in[10] (using the chemical mechanism developed in the same work).

4.3. Reacting cases: soot

Computed soot levels (total soot mass, and spatial distributions) are compared with experimental diagnostics based on measurements of soot optical thickness (*KL*) from high-speed *KL* images obtained using laser extinction and planar laser-induced incandescence.[6,44,45] The experimental field of view for the soot measurements covers the region between 15.2 mm and 67.2 mm downstream of the fuel nozzle exit, and data are available at the ECN database[5] for ambient temperatures of 850 K, 900 K and 1000 K. The measured soot mass is sensitive to the flame lift-off length, since the entire flame is not located within the experimental field of view for low ambient temperatures.

Computed (in the experimental field of view) and measured total soot mass as functions of time for the 900 K ambient temperature case are compared in Fig. 3a–c, and computed and measured spatial distributions of soot volume fraction in the quasi-stationary period (from 2.5 ms to 5.5 ms after SOI) are compared in Fig. 4. Computed results for the 54-species mechanism and two-equation soot model (Fig. 3a) show the strong influence of turbulent fluctuations in composition and temperature on soot levels. The PDF model captures the rapid initial transient rise in soot and subsequent fall off to a quasi-steady value that is observed in the experiments; the WSR model fails to capture the transient. The computed quasi-steady soot mass in the experimental field of view from the PDF model is approximately 50% higher than that from the WSR model, and is in better agreement with experiment. The PDF and WSR spatial distributions of soot are also quite different (Fig. 4). The PDF model produces soot clouds that are qualitatively more consistent with experiment, compared to the WSR model. The PDF model gives lower peak soot levels, and soot clouds that are more compact axially and broader radially compared to the WSR model. The peak soot volume fractions from the WSR model are much higher than the experimentally measured values, and most of the WSR computed soot is downstream of the experimental field of view. It is important to note that, the larger soot mass in the PDF model compared to the WSR model, shown in Fig. 3a–c, arises from the larger radial extent of the soot cloud in the PDF model, which can be seen in Fig. 4b. The soot mass depends on the square of the soot cloud radius, and this prevails over the higher soot volume fraction predicted by the WSR model. There is still room for improvement in the PDF model spatial distributions of soot, and the level of quantitative agreement

between the baseline PDF model and experiment (Fig. 3a) is probably fortuitous, given the uncertainties in soot measurements and the limitations of the chemical mechanism and the soot model. Nevertheless, it is gratifying to find that with no tuning of the soot model or any of the other submodels, this level of agreement with experiment can be realized with a RANS-based formulation when turbulent fluctuations are accounted for using a best-available turbulence–chemistry interaction model.

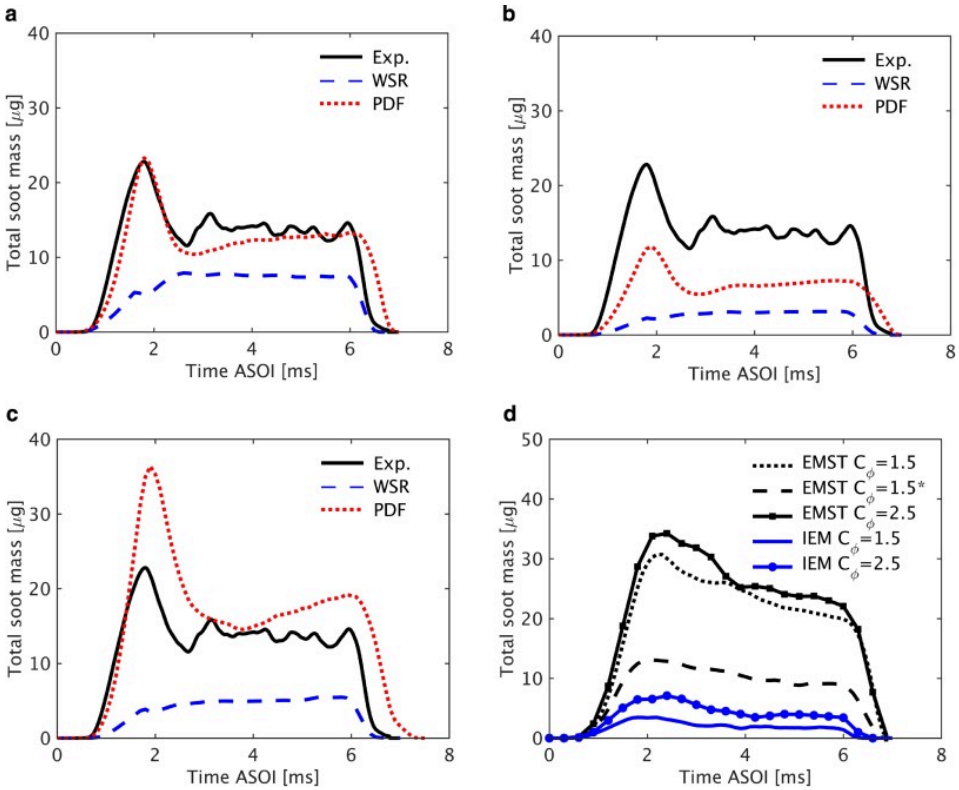

Fig. 3. Measured and computed (using WSR and PDF models) total soot mass versus time after SOI for the 900 K ambient temperature case. In a)–c), the total soot mass in the experimental field of view is shown. In d), the total soot mass in the full vessel is shown. a) 54-species chemical mechanism and two-equation soot model. b) 133-species chemical mechanism and two-equation soot model. c) 133-species chemical mechanism and PAH/MOMIC soot model. d) 54-species chemical mechanism and two-equation soot model, with variations in the PDF mixing model. For the case marked with an asterisk, soot quantities are mixed.

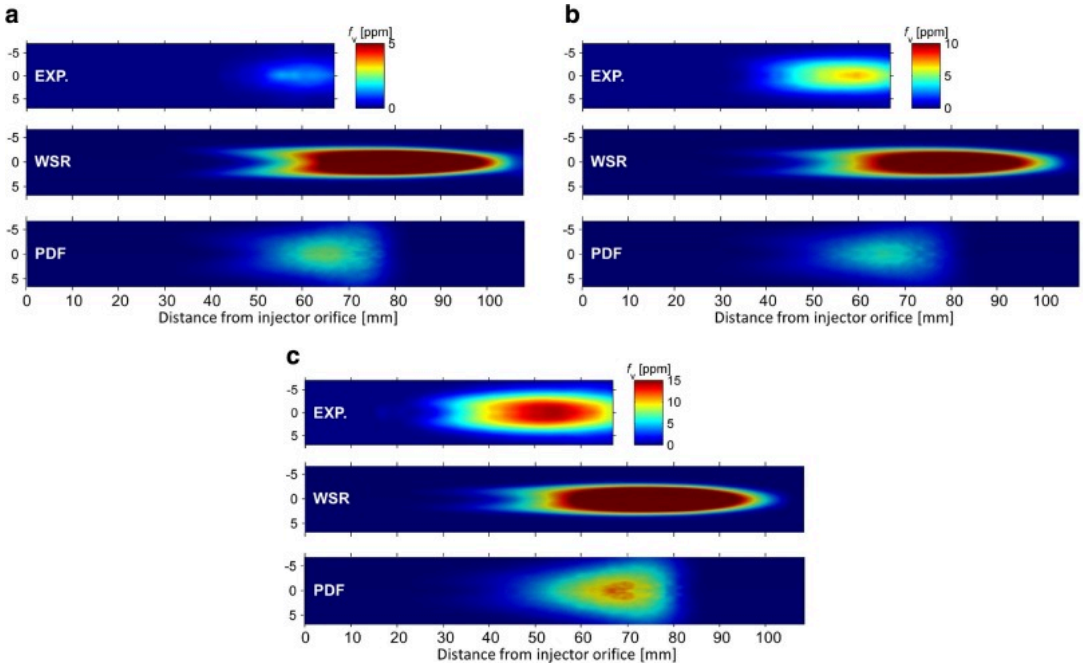

Fig. 4. Measured and computed (WSR and PDF, 54-species chemical mechanism and two-equation soot model) time-averaged (over the quasi-steady period) soot-volume-fraction contours on a cutting plane containing the injection axis. a) T_{amb}= 850 K. b) T_{amb}= 900 K. c) T_{amb}= 1000 K.

To explore the extent to which the results are influenced by the choice of gas-phase chemical mechanism, soot model, and PDF mixing model, results for a 133-species mechanism, a PAH/MOMIC soot model, and several variations in the mixing model are shown in Fig. 3b–d. The 133-species mechanism produces roughly half as much C_2H_2 as the 54-species mechanism (not shown), and the computed soot levels from the 133-species mechanism are approximately half of those from the 54-species mechanism when both are coupled with the same C_2H_2/two-equation soot model (Fig. 3a versus Fig. 3b). The primary target in mechanism development for compression-ignition engines is usually ignition delay time. A factor-of-two (or more) difference in computed C_2H_2 (and other minor species) among different recent n-dodecane mechanisms from the literature is not unusual. Comparisons and discussion of differences among mechanisms can be found in,[25,31] for example. The importance of turbulence–chemistry interactions remains evident in Fig. 3b. When a more detailed soot model is used (Fig. 3c), quantitative differences between the WSR and PDF results are even larger, but again, the same general trends with respect to the transient evolution and turbulence–chemistry interactions are evident. The same 133-species chemical mechanism has been used in Fig. 3b and c. In Fig. 3b, the same C_2H_2-based/two-equation soot model has been used as in Fig. 3a, while the PAH-based/MOMIC soot model has been used in Fig. 3c. The approximately factor-of-two difference in computed soot levels between Fig. 3b and c indicates the extent to which the results vary with the soot model, with all other aspects of the modeling being the same.

Figure 3d shows that the mixing model has a particularly strong influence on computed soot levels. There results for two mixing models (EMST and IEM) are shown for two values of the mixing model coefficient C_ϕ (1.5 and 2.5). For both models, increasing the mixing rate (increasing C_ϕ) yields more soot, and the differences between EMST and IEM are noteworthy. The EMST model enforces locality of mixing in the gas-phase composition space, so that fluid elements having thermochemical states that are

conducive to soot formation tend to remain in a soot-conducive state longer; the computed soot mass from EMST is approximately five times higher than that from IEM, for the same value of C_ϕ. As noted earlier, only gas-phase compositions and mixture-specific enthalpy are mixed, while soot quantities are not mixed (to reflect the high Schmidt number of soot particles). This is also important. As shown in Fig. 3d, the total amount of soot decreases by a factor of two-to-three when soot quantities are mixed (the case indicated with an asterisk).

WSR and PDF model total-soot-mass-versus-time results obtained using the same 54-species chemical mechanism and a similar two-equation soot model were presented for a shorter-injection-duration case in.[13] There the WSR model yielded approximately twice as much soot as the PDF model. Total soot mass predictions from both models were low compared to experiment, by at least a factor of two, and neither model captured the rapid initial transient. The differences with respect to the present results can be attributed to the differences in the mixing model used for the PDF results reported in;[13] IEM was used there. As shown in Fig. 3d, the treatment of mixing has a strong influence on computed soot levels from a PDF model.

Further insight into the differences in soot levels between the PDF and WSR models, especially during the initial transient, is provided in Fig. 5. There computed distributions of in-cylinder fluid mass in equivalence ratio-temperature space are shown at two instants in time for the 900 K ambient temperature case using the 54-species mechanism, with (PDF) and without (WSR) consideration of turbulence–chemistry interactions. Here the equivalence ratio Φ is defined in terms of the mixture fraction *z* as:

$$\Phi = \frac{z}{1-z}, \frac{1-z_{st}}{z_{st}},$$

where Bilger's definition[46] has been used to compute *z*, and z_{st} denotes the stoichiometric value (here $z_{st} = 0.0451$). Both models show evidence of a classic nonpremixed turbulent flame structure, while the PDF model accesses more thermochemical states compared to the WSR model. The "soot region" where soot is expected to form is indicated by the dashed white line (from Fig. 2 of[47]). Approximately 1.3% of the total mass in the vessel is in the flame zone (the region where the temperature is more than 100 K higher than the ambient temperature). A larger fraction of the mixture mass is in the soot region for the PDF model compared to the WSR model. In particular, the PDF model shows more mixture at fuel-rich equivalence ratios between three and four. At the beginning of the steep initial rise in total soot mass (1 ms after SOI), the PDF model mixture mass in the soot region is $\sim$ 60% higher than that for the WSR model; at 3 ms after SOI, this has dropped to $\sim$ 30% higher. The larger mixture mass in the soot region for the PDF model compared to the WSR model, combined with a mixing model that enforces locality in gas-phase composition space and no mixing of soot variables, gives a more rapid initial rise in soot and more total soot (in the experimental field of view) for the PDF model compared to the WSR model.

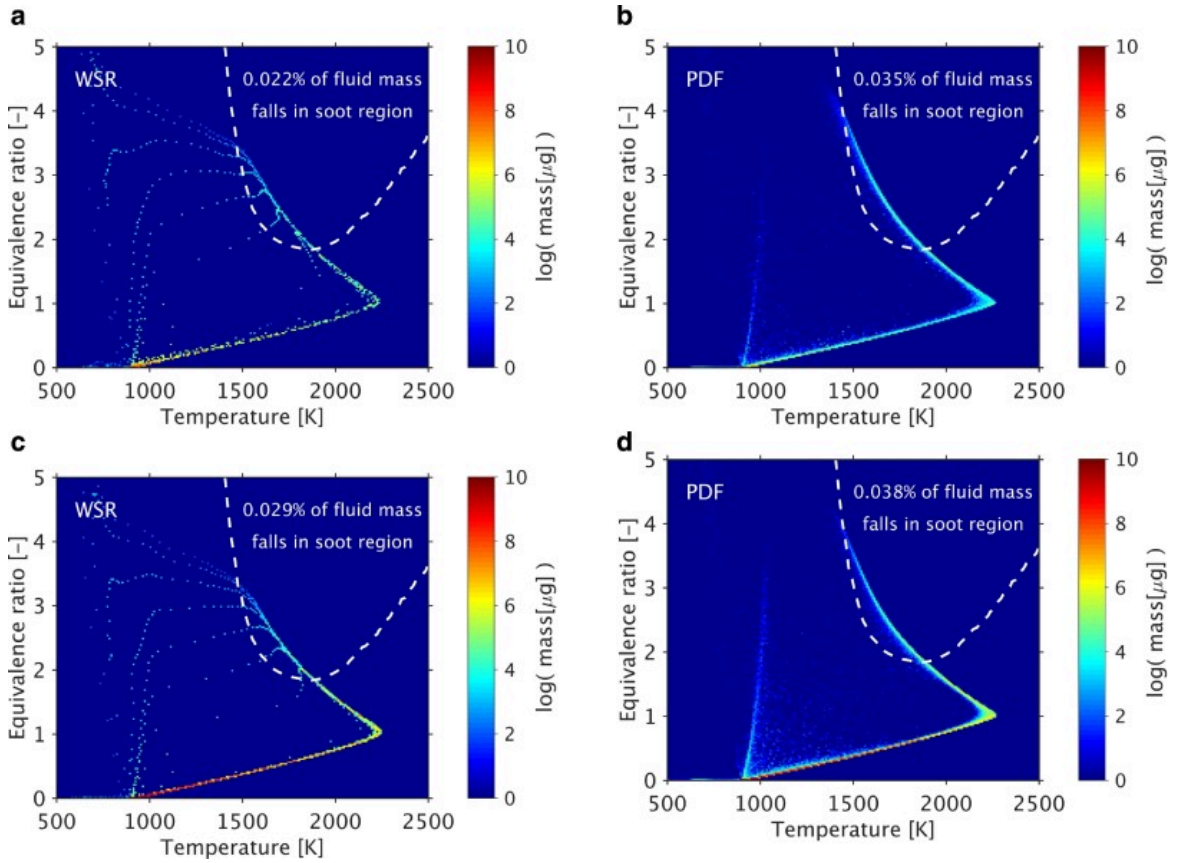

Fig. 5. Computed (54-species mechanism) fluid mass distributions in space at two instants in time for the 900 K ambient temperature case. a) WSR model, 1 ms after SOI. b) PDF model, 1 ms after SOI. c) WSR model, 3 ms after SOI. d) PDF model, 3 ms after SOI.

These results suggest that mixing is at least as important as kinetics in determining the total amount of soot that is formed, and the spatial and temporal evolution of soot, in high-pressure turbulent flames. It is essential to account properly for turbulent fluctuations in composition and temperature, and for the high Schmidt number of soot particles. But apparently it is less important to account for the temporal and spatial coherence of the fluctuations, since the main effects can be captured using URANS (versus large-eddy simulation). The quantitative results vary when a different chemical mechanism and/or a different soot model is used (Fig. 3b and c), but the key conclusions are robust to the specific choice of chemical mechanism and soot model.

Further evidence supporting these conclusions can be found in recent experimental, simulation and modeling studies of soot formation and evolution in high-pressure laminar and turbulent flames. In a diesel-engine modeling study,[48] a PDF model similar to the one used here was shown to produce higher engine-out soot compared to a WSR model (in some cases, by several orders of magnitude) over a range of operating conditions, with the PDF model results being in closer agreement with experiment. As noted in,[34] the sensitivity of computed soot levels in laminar flames to variations in the assumed kinetic rates in a soot model decreases with increasing pressure, because the soot kinetics become faster and less rate-limiting with increasing pressure. The importance of hydrodynamics and scalar dissipation rate (mixing) in soot formation and growth at elevated pressures for coflow laminar diffusion flames is emphasized in.[49] And the high intermittency of soot in turbulent flames has been noted in both

experimental (e.g.,[50]) and DNS (e.g.,[51]) studies of soot processes in turbulent flames. High soot intermittency is realized with the present PDF model through the combination of the EMST mixing model for gas-phase species and no mixing for soot. This is discussed further in the following subsection.

4.4. Reacting cases: spectral radiative heat transfer

Radiative heat transfer has been neglected in all of the modeling results presented up to this point in this paper. A limited number of runs were made with coupled radiation models for the 900 K ambient temperature case to gauge the global importance of radiative transfer on flame structure (e.g., ignition delay and lift-off length) and soot levels. The maximum changes were for the extreme case of an optically thin PDF odel. (The system is, in fact, far from being optically thin, as will be shown in what follows.) There the computed lift-off length increased by approximately 1.8 mm and the computed soot mass decreased by less than 10%, compared to the no-radiation case. These differences presumably are consequences of the small drop in temperature resulting from radiative heat loss. The modest global effects of radiation for this configuration are not surprising, given the small size of the flame compared to the volume of the combustion vessel. The radiant fractions are quite small, as will be discussed later. Nevertheless, a detailed analysis of spectral radiation for this system provides valuable insight into the nature of radiative heat transfer in high-pressure turbulent combustion systems with soot, such as in piston engines. The small global effects of radiation allow this analysis to be performed by post-processing of results from simulations that did not include a coupled radiation model. Most of the analysis that follows is for the 900 K ambient temperature case at an instant in time during the quasi-steady period (3 ms after SOI).

Computed mean and rms fields of several quantities that contribute to radiative emission and reabsorption are shown in Fig. 6. The full radial extent of the computational domain is not shown, so that the flame structure can be seen more clearly. The two principal participating molecular gases (CO_2 and H_2O) are at different spatial locations in the flame, with the region of highest H_2O being inside (toward the fuel-rich side) the region of highest CO_2. It is important to note that both CO_2 and H_2O are nonzero in the ambient mixture, outside of the flame. Most of the soot is limited to a compact region toward the head of the flame. And high temperatures coincide with high CO_2. The highest fluctuations (rms values) in CO_2, H_2O and T generally coincide with the steepest gradients in the corresponding mean contours, as expected. However, the rms soot volume fraction shows very different behavior. For soot, the rms values are higher than the mean values at most locations, and the spatial extent of the rms soot field is broader than that of the mean soot field. This reflects the highly intermittent nature of the soot in the turbulent flame, which is captured in the PDF model through the combination of the EMST mixing model for gas-phase species and no mixing for soot.

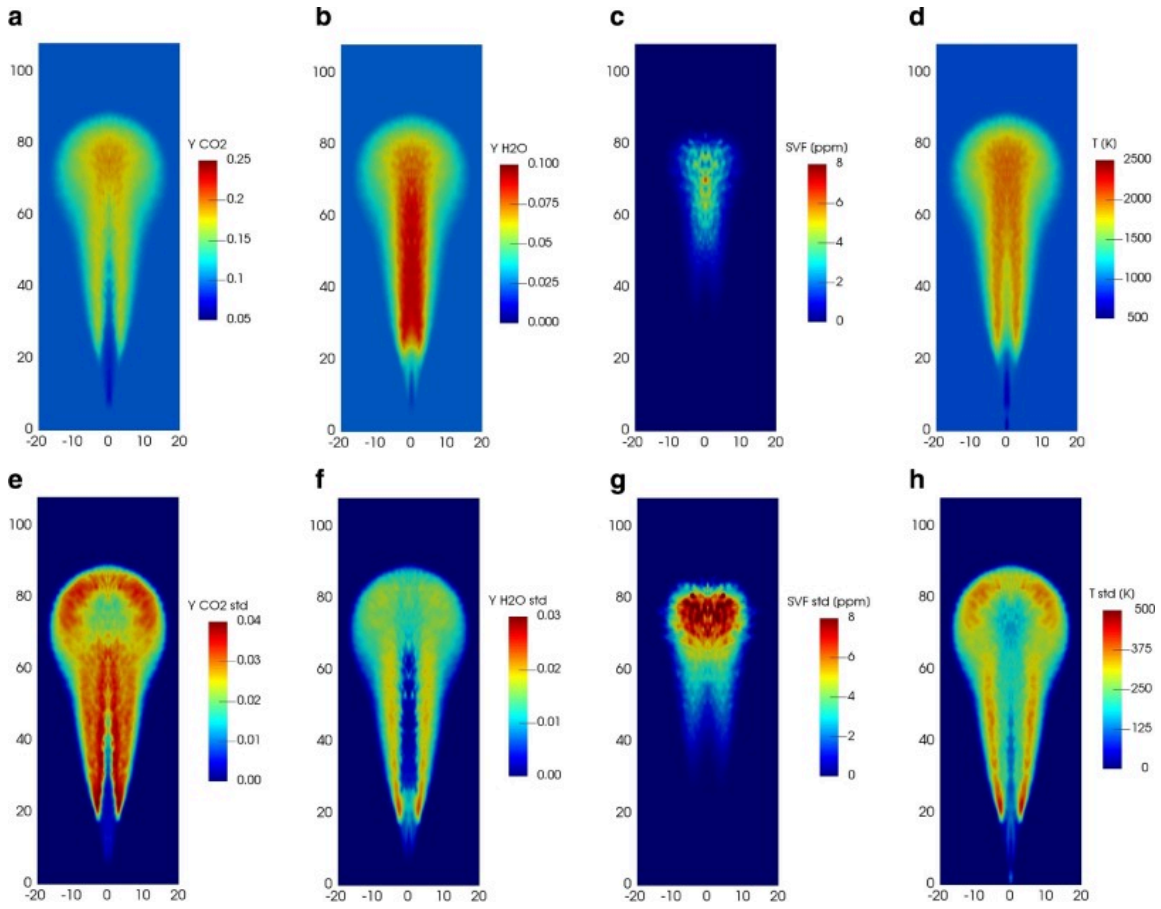

Fig. 6. Computed contours of mean and rms radiatively participating species and temperature on a cutting plane containing the injection axis at 3 ms after SOI. Results are for the 900 K ambient temperature case, using the baseline PDF model. a) Mean CO_2 mass fraction. b) Mean H_2O mass fraction. c) Mean soot volume fraction. d) Mean temperature. e) Rms CO_2 mass fraction. f) Rms H_2O mass fraction. g) Rms soot volume fraction. h) Rms temperature.

A PMC/LBL radiation model is used to compute radiative emission and reabsorption. Three participating molecular gases are considered (CO_2, H_2O and CO), plus soot. As discussed earlier, radiation can be computed using PDF notional particle values of composition and temperature, thereby accounting for the influence of unresolved turbulent fluctuations on radiation ("turbulence-radiation interactions" – TRI), or using the local mean values of composition and temperature, thereby neglecting the influence of unresolved turbulent fluctuations on radiation (no TRI). Turbulence–chemistry interactions are included in all cases, since the post-processing is performed for a PDF model case. Computed fields of radiative emission and net radiative source term (absorption minus emission) are shown in Fig. 7. There the computed radiative source term fields with and without consideration of TRI are shown, and the chemical heat release term is also shown for comparison. The chemical source term peaks at the base of the flame, and has a maximum value that is approximately three orders of magnitude higher than the maximum value of the radiative source term. The spatial distribution of the radiative source term is similar to that of CO_2 and temperature (Fig. 6). TRI effects (emission TRI in Fig. 7d, total TRI in Fig. 7h) are most prominent at the periphery of the turbulent flame, especially in the area corresponding to the highly intermittent soot cloud (Fig. 6g).

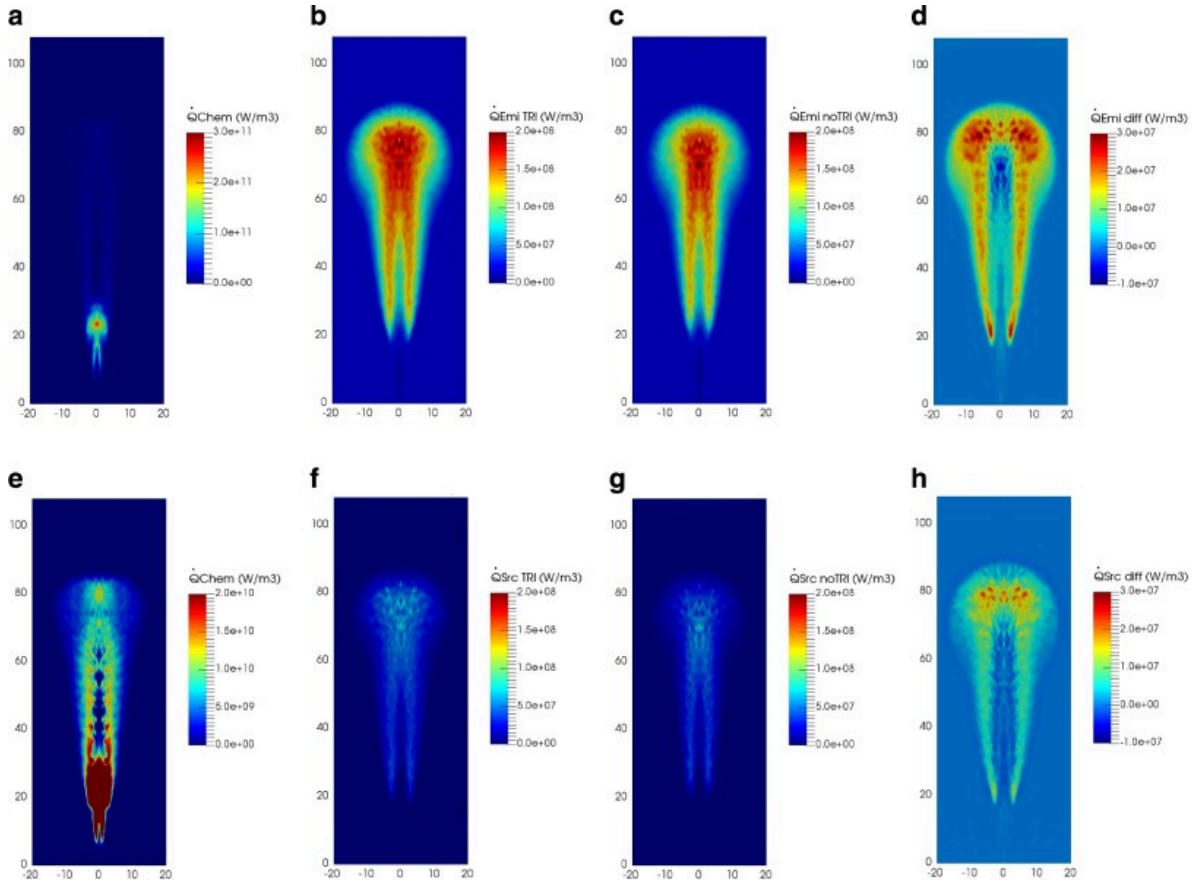

Fig. 7. Computed contours of source terms in the mean sensible enthalpy equation on a cutting plane containing the injection axis at 3 ms after SOI. Results are for the 900 K ambient temperature case, using the baseline PDF model. a) Chemical source term. b) Radiative emission based on notional PDF particle values (with TRI). c) Radiative emission based on local mean values (no TRI). d) Difference c) and d). e) Chemical source term (same as a), rescaled to show the downstream spatial structure more clearly. f) Radiative source term (absorption - emission) based on notional PDF particle values (with TRI). g) Radiative source term (absorption - emission) based on local mean values (no TRI). h) Difference f) and g).

The total radiative emission and total radiative reabsorption, and the percentage contributions from each of the three molecular gases and from soot to emission, reabsorption and radiation reaching the walls are summarized in Table 2. The radiative power that reaches the walls is the difference between the total emission and the total reabsorption. To separate the radiative effects of the ambient gas from those of the turbulent flame itself, results are shown for the full computational domain and for a case where radiation is computed for the flame-zone only. For the latter, no emission or reabsorption is computed if the local mean temperature is less than 1000 K. In addition, to isolate and quantify TRI effects, results are shown with radiation computed based on notional PDF particle values of composition and temperature (with TRI) and with radiation computed based on local mean values of composition and temperature (no TRI).

Table 2. Total radiative emission and total radiative reabsorption, and percentage contributions from individual species to emission, reabsorption and radiative power reaching walls. Values are from PMC/LBL postprocessing of a baseline PDF model run for the 900 K ambient temperature case at 3.0 ms after SOI. Results are shown with and without consideration of TRI, and for two domains: the full combustion chamber, and the flame zone only.

TRI, domain considered	**Total emission, total absorption**	**Species**	**% of emission**	**% of absorption**	**% of radiation reaching walls**
		CO_2	87.46	90.62	35.88
No TRI,	207,43 W,	H_2O	12.19	9.29	59.56
full domain	19,545 W	CO	0.06	0.05	0.29
		Soot	0.29	0.04	4.27
		CO_2	87.02	90.49	33.81
With TRI,	21,073 W,	H_2O	12.29	9.36	57.22
full domain	19,783 W	CO	0.07	0.06	0.30
		Soot	0.62	0.09	8.67
		CO_2	79.83	85.89	17.44
No TRI,	1843 W,	H_2O	16.20	12.99	49.24
flame zone	1680 W	CO	0.71	0.58	2.09
		Soot	3.26	0.54	31.23
		CO_2	76.52	85.07	13.75
With TRI,	2131 W,	H_2O	16.63	13.31	40.98
flame zone	1875 W	CO	0.73	0.62	1.53
		Soot	6.12	1.00	43.74

Several observations can be made from Table 2. 1) The flame zone accounts for less than 10% of the total emission and total reabsorption; ambient-mixture CO_2 (and to a lesser extent, H_2O) radiation dominates the radiative emission and reabsorption in the vessel. 2) While CO_2 dominates the radiative emission, the system is quite optically thick at the wavenumbers that prevail for CO_2 radiation (more on that later), and the radiation that reaches the walls is dominated by H_2O radiation. The main influence of CO_2 radiation is to redistribute energy spatially within the combustion chamber. 3) Very little of the soot radiation emitted is reabsorbed before reaching the walls, but soot still accounts for less than 10% of the radiation that reaches the walls. 4) When the analysis is limited to flame-zone radiation only, the

relative contribution of soot radiation is higher, and the contributions of soot and H_2O to the radiation that reaches the walls are approximately equal (with TRI). 5) Both total emission and total reabsorption increase with consideration of TRI, but the net effect of TRI is small: 1–2% for the full domain, or 10–15% for the flame zone. 6) However, the contribution of TRI to soot radiation is significant: soot emission approximately doubles with consideration of TRI. This is a consequence of the highly intermittent nature of the soot in the turbulent flame, as discussed earlier.

Further insight is provided in Fig. 8. There two sets of radiation power spectra are shown: one for the total radiative emission over the full computational domain (Fig. 8a), and the other for all of the radiative energy that reaches the walls of the domain (Fig. 8b). Here CO radiation has been omitted, for clarity. The broadband spectrum of soot particle emission (peaking in the near infrared for these temperatures) is evident, as is the spectral band radiation for the two molecular gases; there is considerable band broadening in this approximately 60 bar system. Two noteworthy bands are the dominant 4.2 μm band for CO_2, and the overlapping CO_2 and H_2O bands at $\sim$ 2.8 μm. The spectrum of radiation reaching the walls differs significantly from that of the total emitted radiation, because of reabsorption in (primarily) the CO_2 and H_2O bands. Three key differences are: the 4.2 μm CO_2 band is strongly attenuated (the system is extremely optically thick at that wavelength); the 2.8 μm CO_2/H_2O overlap band is also strongly attenuated; and the soot spectrum reaching the walls has prominent aps over these two wavenumber bands, in particular, although the overall attenuation of the soot radiation is small (Table 2). This suggests that a relatively simple CFD-based model for radiative heat transfer under these conditions might be devised to account for both the spatial redistribution of energy within the vessel and radiative heat losses to the walls. A starting point would be an optically thin approximation for soot (including emission TRI), and a model for molecular gas radiation that considers as few as two bands for CO_2 and one for H_2O, with a simple radiative transfer equation (RTE) solver such as the P1 method.[37] P1 is expected to be compatible with the relatively optically thick nature of the molecular gas radiation at high pressures.

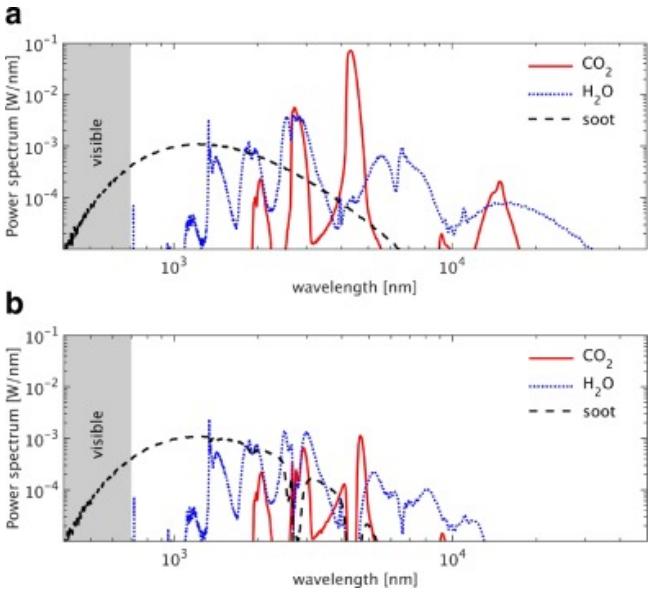

Fig. 8. Computed power spectra of radiation for the 900 K ambient temperature case. Results are from PMC/LBL postprocessing of a snapshot from a baseline PDF model solution 3 ms after SOI. a) Spectrum of radiation emitted over the full domain. b) Spectrum of radiation reaching walls.

A radiant fraction χ is defined as the ratio of the radiative energy emitted from a flame to the chemical (fuel) energy supplied to the flame. Spray A radiant fraction measurements were reported in.[14] There radiation was measured over visible wavelengths between 360 and 700 nm, and an assumed soot spectrum was used to extrapolate to total soot radiation. Therefore, the measured radiant fractions correspond to soot radiation only (see Fig. 8). Computed and measured radiant fractions for ambient temperatures from 850 K to 1200 K are compared in Fig. 9. There two computed values of χ are shown: one based on all radiation reaching the walls, and the other based on the soot radiation reaching the walls. The computed total radiant fraction is more than 20 times higher than the computed soot radiant fraction at 850 K, but the soot contribution to radiation increases with increasing ambient temperature, and the ratio is approximately a factor of three at 1200 K. The computed and measured soot radiant fractions agree to within 2% for ambient temperatures of 900 K and 1000 K (again, this level of quantitative agreement is probably fortuitous), but the computed values increase faster than the measured values at higher temperatures, presumably because soot is overpredicted at the higher temperatures.

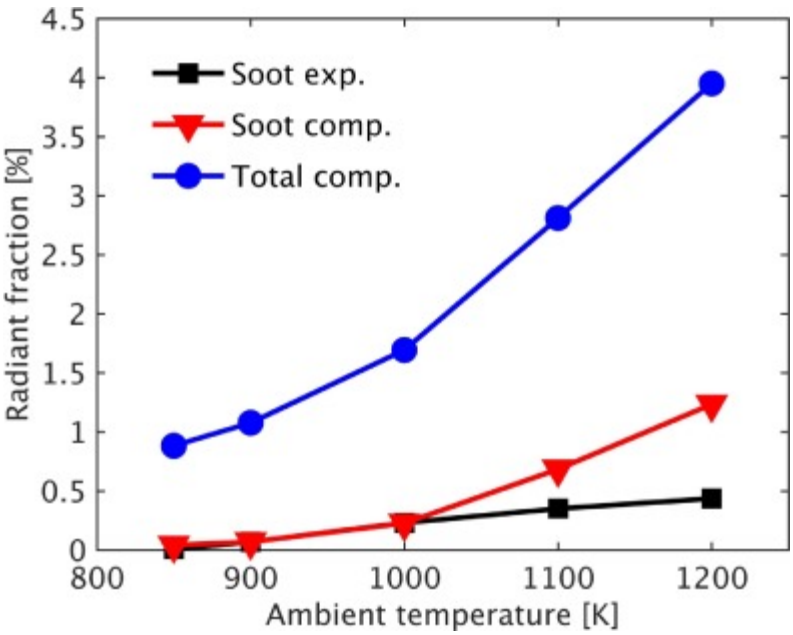

Fig. 9. Measured[14] and computed radiant fractions versus ambient temperature. Computed values are from PMC/LBL postprocessing from a baseline PDF model solution, over the time interval 0.0–5.5 ms after SOI. Two computed values are shown: one for the soot radiation reaching the walls, and the other for the total radiation reaching the walls.

Finally, computed spatially and spectrally resolved radiative intensities for the 900 K ambient temperature case are compared to experimental measurements of the same[14] in Fig. 10. In the experiments, spectrally resolved measurements of radiative intensities over visible wavelengths between 360 nm and 700 nm (soot radiation) were measured as a function of axial distance from the injector orifice over the quasi-stationary period. The intensity is highest at the axial location corresponding to the peak soot volume fraction: approximately 60 mm downstream of the injector orifice. At each axial location, the spectral variation is consistent with the visible wavelengths of the broadband soot radiation (approximately a blackbody distribution). The bright horizontal streak in the experimental figure at approximately 40 mm is a measurement artifact, as discussed in.[14]

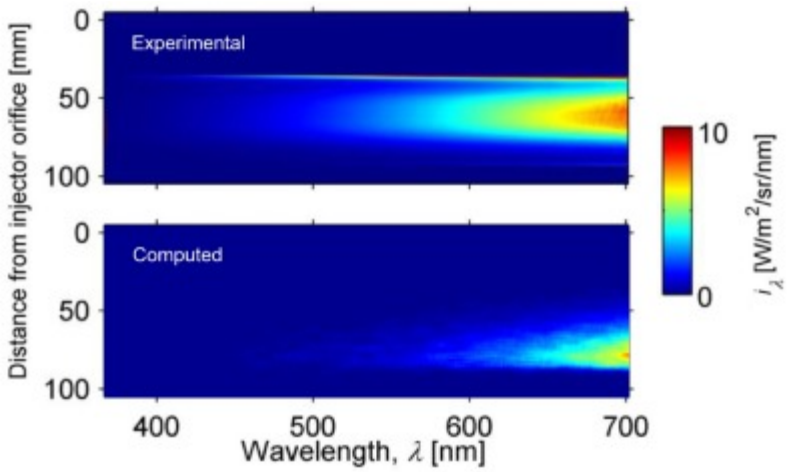

Fig. 10. Measured[14] and computed (PMC/LBL postprocessing of the baseline PDF model) spatially and spectrally resolved radiative intensities for the 900 K ambient temperature case.

To compute a quantity that is approximately equivalent to what was measured experimentally, the PMC/LBL data have been post-processed as follows. The domain is divided into bins in the axial direction (the injection direction). For each bin, the local soot cloud radius is calculated, using a threshold of 0.1 ppm. The local soot cloud area is then calculated based on the local soot cloud radius and the axial bin length. The spectral intensity for each axial bin is then calculated from the spectral emission power within the local soot cloud and the local soot cloud area. The computed location of peak intensity is downstream of the experimentally measured peak, consistent with the difference between the measured and computed soot cloud locations (Fig. 4). The overall computed intensity levels are somewhat lower than the measured values, which may reflect different assumptions regarding the index of refraction of soot particles in the visible wavelengths or other differences in processing the data between the experiments and the simulations, but the relative spectral intensity distributions are essentially the same as in the experiments.

This is a first step toward making direct quantitative comparisons of computed and measured spectral radiative intensities corresponding to various optical diagnostic techniques. It is anticipated that such comparisons will facilitate making quantitative comparisons between simulations and experiments, as it has the potential to reduce the assumptions that are required to extract quantitative values of soot volume fraction (and other quantities) from optical-diagnostics-based experimental methods.

5. Conclusions

A transported PDF method and a PMC/LBL radiation model have been exercised to generate physical insight into soot formation/evolution processes and spectral radiation characteristics of transient high-pressure turbulent n-dodecane spray flames (ECN Spray A). PDF model results have been compared with experimental measurements and with results from a WSR model that neglects the effects of unresolved turbulent fluctuations in composition and temperature. Key findings are as follows.

- Differences between computed ignition delays and lift-off lengths from the PDF and WSR models are small for ambient temperatures of 900 K and higher; both models give results that are within a few percent of the measured values. The differences between the models, and between the models and experiment, increase with decreasing ambient temperature, with the

extent of the differences depending on the chemical mechanism used. The lower-temperature differences tend to be more significant for the lift-off length than for the ignition delay, with the PDF model results being closer to experiment. These results largely confirm what has been shown in earlier modeling studies that focused on turbulence-chemistry interactions in these flames.[9,10,11,12]

• In soot modeling, it is essential to account for the influences of unresolved turbulent fluctuations in composition and temperature. Accounting for the spatial and temporal coherence of the fluctuations may be of secondary importance, since the main effects with respect to overall soot levels and soot spatial distributions appear to be captured in URANS/PDF.

• It is equally important to account for the high Schmidt number of soot particles. In general, soot kinetics are fast at high pressure, and mixing is at least as important as kinetics in controlling soot formation and evolution in high-pressure turbulent flames. The EMST mixing model, with no mixing of soot variables, allows important physical aspects of mixing to be represented, and captures the highly intermittent character of the soot in the turbulent flame. This is the only RANS-based model to date that has reproduced the rapid initial soot transient that is observed experimentally in these flames.

• While the level of quantitative agreement between computed and measured total soot mass for the baseline model (Fig. 3a) is probably fortuitous, it is nonetheless noteworthy that no tuning of the soot model or of other physical models has been done to match the soot measurements. The conclusions regarding the importance of turbulent fluctuations and mixing are robust to the specific choice of chemical mechanism and soot model, although the quantitative results vary depending on the specific models used.

• Radiant fractions and global radiation effects in these flames are small (small flames in a large vessel, and ambient mixtures that contain radiatively participating molecular gases). Most of the emitted soot radiation reaches the walls. Computed soot radiant fractions are within 2% of the experimentally measured values for ambient temperatures of 900 K and 1000 K, but computed soot radiant fractions increase faster than the measured values with increasing ambient temperature.

• Consideration of spectral radiation properties is essential to understand radiative heat transfer in these flames. There are complex spectral interactions that would be difficult, if not impossible, to unravel without PMC/LBL. While radiative emission is dominated by CO_2, radiation reaching the walls is dominated by H_2O. When radiation from the ambient mixture is ignored, H_2O and soot radiation contribute approximately equally to the radiation reaching the walls for the 900 K ambient temperature case.

• Global TRI effects are small (< 10%), because of the large volume of ambient mixture containing CO_2 and H_2O with essentially no fluctuations. However, radiative emission from soot approximately doubles with consideration of TRI, because of the highly intermittent soot distribution.

• Radiation contributes to the spatial redistribution of energy in the vessel, in addition to contributing to heat losses from the system. The results suggest that a reasonable starting point for a CFD-based model for radiative heat transfer in engine-relevant conditions might be an optically thin model for soot (including emission TRI), plus consideration of the 4.2 μm CO_2 band and the main CO_2/H_2O overlap band at $\sim$ 2.8 μm using a simple RTE solver such as P1.

Acknowledgments

This research has been funded by the U.S. National Science Foundation through grants CBET-1258613 and CBET-1604446 (Haworth) and CBET-1258635 (Modest). Funding was also provided by the Department of Energy, Office of Energy Efficiency and Renewable Energy (EERE) and the Department of Defense, Tank and Automotive Research, Development, and Engineering Center (TARDEC), under Award Number DE-EE0007278. The authors are grateful for the opportunity to discuss aspects of this work with colleagues at the Engine Combustion Network Workshops. In particular, we thank Drs. Scott Skeen and Lyle Pickett of Sandia National Laboratories, and Prof. Evatt Hawkes of the University of New South Wales.

References

1. R.D. Reitz. **Directions in internal combustion engine research.** Combust. Flame, 160 (2013), pp. 1-8
2. A workshop to identify research needs and impacts in predictive simulation for internal combustion engines (preSICE), Office of science and office of energy and renewable energy, 2011, U.S. Department of Energy. Available at https://science.energy.gov/~/media/bes/pdf/reports/files/PreSICE_rpt.pdf.
3. C. Paul, A. Sircar, S. Ferreyro-Fernandez, A. Imren, D.C. Haworth, S. Roy, Ge W., M.F. Modest. **Modeling radiative heat transfer and turbulence–radiation interactions in engines.** 10th U.S. National Combustion Meeting, College Park, MD (2017) 23–26 April
4. M.F. Modest, D.C. Haworth. **Radiative heat transfer in turbulent combustion systems: theory and applications.** Springer (2016)
5. Engine Combustion Network, available at https://ecn.sandia.gov (2017).
6. M.P.B. Musculus, L.M. Pickett. **Diagnostic considerations for optical laser-extinction measurements of soot in high-pressure transient combustion environments.** Combust. Flame, 141 (2005), pp. 371-391
7. L.M. Pickett, C.L. Genzale, G. Bruneaux, L.-M. Malbec, L. Hermant, C. Christiansen, J. Schramm. **Comparison of diesel spray combustion in different high-temperature, high-pressure facilities.** SAE Int. J. Engines, 3 (2010), pp. 2156-2181
8. Engine Combustion Network: Spray A&B, available at https://ecn.sandia.gov/diesel-spray-combustion/target-condition/spray-ab/ (2017).
9. S. Bhattacharjee, D.C. Haworth. **Simulations of transient n-heptane and n-dodecane spray flames under engine-relevant conditions using a transported PDF method.** Combust. Flame, 160 (2013), pp. 2083-2102
10. Pei Y., E.R. Hawkes, S. Kook, G.M. Goldin, Lu T.. **Modelling n-dodecane spray and combustion with the transported probability density function method.** Combust. Flame, 162 (2015), pp. 2006-2019
11. Pei Y., E.R. Hawkes, M. Bolla, S. Kook, G.M. Goldin, Yang Y., S.B. Pope, S. Som. **An analysis of the structure of an n-dodecane spray flame using TPDF modelling.** Combust. Flame, 168 (2016), pp. 420-435

12. M. Bolla, M.A. Chishty, E.R. Hawkes, Chan Q.N., S. Kook. **Influence of turbulent fluctuations on radiation heat transfer, NO and soot formation under ECN Spray A conditions.** Proc. Combust. Inst., 36 (2017), pp. 3551-3558
13. S.A. Skeen, J. Manin, L.M. Pickett, E. Cenker, G. Bruneaux, K. Kondo, T. Aizawa, F. Westlye, K. Dalen, A. Ivarsson, Xuan T., J.M. Garcia-Oliver, Pei Y., S. Som, Hu W., R.D. Reitz, T. Lucchini, G. D'Errico, D. Farrace, S.S. Pandurangi, Y.M. Wright, M.A. Chishty, M. Bolla, E.R. Hawkes. **A progress review on soot experiments and modeling in the engine combustion network (ECN).** SAE Int. J. Engines, 9 (2016), pp. 883-898
14. S.A. Skeen, J. Manin, L.M. Pickett, K. Dalen, A. Ivarsson, Quantitative spatially resolved measurements of total radiation in high-pressure spray flames, 2014, SAE Technical Paper 2014-01-1252.
15. L.M. Pickett, J. Manin, C.L. Genzale, D.L. Siebers, M.P.B. Musculus, C.A. Idicheria. **Relationship between diesel fuel spray vapor penetration/dispersion and local fuel mixture fraction.** SAE Int. J. Engines, 4 (2011), pp. 764-799
16. OpenFOAM open source software for computational fluid dynamics, available at http://www.openfoam.org (2016).
17. S.H.E. Tahry**ε. equation for compressible reciprocating engine flows.** AIAA J. Energy, 7 (1983), pp. 345-353
18. S. James, M.S. Anand, M.K. Razdan, S.B. Pope. **In situ detailed chemistry calculations in combustion flow analyses.** J. Eng. Gas Turb. Power, 123 (2001), pp. 747-756
19. Han Z., S. Parrish, P.V. Farrell, R.D. Reitz. **Modeling atomization processes of pressure swirl hollow-cone fuel sprays.** At. Sprays, 7 (1997), pp. 663-684
20. L. Allocca, G. Bella, A. De Vita, L.D. Angelo, Experimental validation of a GDI spray model, 2002, SAE Technical Paper 2002-01-1137.
21. J.K. Dukowicz. **A particle-fluid numerical model for liquid sprays.** J. Comput. Phys., 35 (1980), pp. 229-253
22. R.D. Reitz. **Modelling atomization processes in high pressure vaporizing sprays.** At. Spray Technol., 3 (1987), pp. 309-377
23. R.D. Reitz, R. Diwakar, Effect of drop breakup on fuel sprays, 1986, SAE Technical Paper 860469.
24. R.D. Reitz, R. Diwakar, Structure of high-pressure fuel sprays, 1987, SAE Technical Paper 870598.
25. Yao T., Pei Y., Zhong B.-J., S. Som, Lu T., Luo K.H. **A compact skeletal mechanism for n-dodecane with optimized semi-global low-temperature chemistry for diesel engine simulations.** Fuel, 191 (2017), pp. 339-349
26. Leung K.M., R.P. Lindstedt, W.P. Jones. **A simplified reaction mechanism for soot formation in nonpremixed flames.** Combust. Flame, 87 (1991), pp. 289-305
27. Guo H., Liu F., G.J. Smallwood. **Soot and NO formation in counterflow ethylene/oxygen/nitrogen diffusion flames, combust.** Theory Model., 8 (1991), pp. 475-489
28. S. Subramaniam, S.B. Pope. **A mixing model for turbulent reactive flows based on Euclidean minimum spanning trees.** Combust. Flame, 115 (1998), pp. 487-514
29. D.C. Haworth. **Progress in probability density function methods for turbulent reacting flows.** Prog. Energy Combust. Sci., 36 (2010), pp. 168-259

30. C.K. Westbrook, W.J. Pitz, O. Herbinet, H.J. Curran, E.J. Silke. **A detailed chemical kinetic reaction mechanism for n-alkane hydrocarbons from n-octane to n-hexadecane.** Combust. Flame, 156 (1) (2009), pp. 181-199
31. A. Frassoldati, G.D. Errico, T. Lucchini, A. Stagni, A. Cuoci, T. Faravelli, A. Onorati, E. Ranzi. **Reduced kinetic mechanisms of diesel fuel surrogate for engine CFD simulations.** Combust. Flame, 162 (2015), pp. 3991-4007
32. A. Imren, D.C. Haworth. **On the merits of extrapolation-based stiff ODE solvers for combustion CFD.** Combust. Flame, 174 (2016), pp. 1-15
33. M. Frenklach. **Method of moments with interpolative closure.** Chem. Eng. Sci., 57 (2002), pp. 2229-2239
34. S.P. Roy, D.C. Haworth. **A systematic comparison of detailed soot models and gas-phase chemical mechanisms in laminar premixed flames.** Combust. Sci. Technol., 188 (2016), pp. 1021-1053
35. J. Villermaux, J.C. Devillon. **Représentation de la coalescence et de la redispersion des domaines de ségrégation dans un fluide par un modèle d'interaction phénoménologique.** Proceedings of the Second International Symposium on Chemical Reaction Engineering, Elsevier, New York (1972), pp. 1-13
36. G. Pal, A. Gupta, M.F. Modest, D.C. Haworth. **Comparison of accuracy and computational expense of radiation models in simulation of non-premixed turbulent jet flames.** Combust. Flame, 162 (2015), pp. 2487-2495
37. M.F. Modest. **Radiative heat transfer.** (second), Academic Press, New York (2003)
38. Wang A., M.F. Modest. **Photon Monte Carlo simulation for radiative transfer in gaseous media represented by discrete particle fields.** J. Heat Trans., 128 (2006), pp. 1041-1049
39. L.S. Rothman, I.E. Gordon, R.J. Barber, H. Dothe, R.R. Gamache, A. Goldman, V. Perevalov, S.A. Tashkun, T.J. HITEMP. **The high-temperature molecular spectroscopic database.** J. Quant. Spect. Rad. Trans., 111 (2010), pp. 2139-22150
40. Chang H., T. Charalampopoulos. **Determination of the wavelength dependence of refractive indices of flame soot.** Proc. R. Soc., 430 (1990), pp. 557-591
41. CMT-Motores Trmicos. Universitat Politcnica de Valncia, available at http://www.cmt.upv.es/ECN03.aspx, 2013.
42. Engine Combustion Network: ECN5 Proceedings, available at https://ecn.sandia.gov/ecn-workshop/ecn5-workshop/, 2017.
43. S. Som, D.E. Longman, Luo Z., M. Plomer, Lu T. **Three dimensional simulations of diesel sprays using n-dodecane as a surrogate.** Fall Technical Meeting of the Eastern States Section of the Combustion Institute, Storrs, CT (2011), pp. 9-11 October
44. L.M. Pickett, D.L. Siebers. **Soot in diesel fuel jets: effects of ambient temperature, ambient density, and injection pressure.** Combust. Flame, 138 (2004), pp. 114-135
45. F.R. Westlye, K. Penney, A. Ivarsson, L.M. Pickett, J. Manin, S.A. Skeen. **Diffuse back-illumination setup for high temporally resolved extinction imaging.** Appl. Opt., 56 (2017), pp. 5028-5038
46. R.W. Bilger, S.H. Starner, Kee R.J. **On reduced mechanisms for methane–air combustion in nonpremixed flames.** Combust. Flame, 80 (1990), pp. 135-149

47. J.E. Dec. **Advanced compression-ignition engines – understanding the in-cylinder processes.** Proc. Combust. Inst., 32 (2009), pp. 2727-2742
48. V.R. Mohan, D.C. Haworth. **Turbulence–chemistry interactions in a heavy-duty compression-ignition engine.** Proc. Combust. Inst., 35 (2015), pp. 3053-3060
49. A. Abdelgadir, I.A. Rakha, S.A. Steinmetz, A. Attili, F. Bisetti, W.L. Roberts. **Effects of hydrodynamics and mixing on soot formation and growth in laminar coflow diffusion flames at elevated pressures.** Combust. Flame, 181 (2017), pp. 39-53
50. Lee S.-Y., S.R. Turns, R.J. Santoro. **Measurements of soot, OH, and PAH concentrations in turbulent ethylene/air jet flames.** Combust. Flame, 156 (2009), pp. 2264-2275
51. F. Bisetti, G. Blanquart, M.E. Mueller, H. Pitsch. **On the formation and early evolution of soot in turbulent nonpremixed flames.** Combust. Flame, 159 (2012), pp. 317-335